Secondary instabilities in breaking inertia-gravity waves

Mark D. Fruman * and Ulrich Achatz

Institute for Atmospheric and Environmental Sciences, Goethe University Frankfurt, Germany

* *Corresponding author address:* M. D. Fruman, IAU, Goethe Universität-Frankfurt, Altenhöferallee 1, 60438 Frankfurt am Main, Germany.

E-mail: fruman@iau.uni-frankfurt.de

ABSTRACT

The three-dimensionalization of turbulence in the breaking of nearly vertically propagating inertia-gravity waves is investigated numerically using singular vector analysis applied to the Boussinesq equations linearized about three two-dimensional time-dependent basic states obtained from nonlinear simulations of breaking waves: a statically unstable wave perturbed by its leading transverse normal mode, the same wave perturbed by its leading parallel normal mode, and a statically stable wave perturbed by a leading transverse singular vector. The secondary instabilities grow through interaction with the buoyancy gradient and velocity shear in the basic state. Which growth mechanism predominates depends on the time dependent structure of the basic state and the wavelength of the secondary perturbation. The singular vectors are compared to integrations of the linear model using random initial conditions, and the leading few singular vectors are found to be representative of the structures that emerge in the randomly initialized integrations. A main result is that the length scales of the leading secondary instabilities are an order of magnitude smaller than the wavelength of the initial wave, suggesting that the essential dynamics of the breaking might be captured by tractable nonlinear three-dimensional simulations in a relatively small triply periodic domain.

1. Introduction

The importance of gravity waves to the large scale circulation in the middle atmosphere is well established. The mean state of the atmosphere as well as phenomena such as the cold summer pole in the mesopause (Houghton 1978) and the quasi-biennial oscillation (QBO) in equatorial winds in the stratosphere (Lindzen and Holton 1968) cannot be properly explained without accounting for the effects of gravity waves.

The range of scales inherent in the sources of gravity waves in the middle atmosphere, especially flow over topography and convection but also spontaneous emission from the

adjustment of balanced flows, is reflected in the range of temporal and spatial scales involved, from minutes to several hours and tens of metres to thousands of kilometres (see Fritts et al. 2006, for a review of the characteristics of gravity wave sources). Due to the range of scales involved, both the sources of gravity waves and the momentum deposition associated with their breaking, known as gravity-wave drag, must be at least partially parameterized in general circulation models.

Most parameterization schemes, such as that of Lindzen (1981) and Holton (1982), are based on the criterion of static instability (also known as convective instability). Gravity waves from a source with prescribed wavenumber and frequency spectrum are assumed to propagate vertically against a mean background wind and temperature field. The propagation of the waves is assumed to follow the predictions of WKBJ theory (Bretherton 1966; Grimshaw 1975; Müller 1976), wherein the frequency, vertical wavenumber and amplitude of the waves vary depending on the structure of the background fields. At the point at which the waves become statically unstable, i.e. where the total potential temperature field decreases locally with height, some or all of the momentum of the waves is absorbed by the mean flow and the amplitude of the waves as they continue upward is reduced relative to the growth predicted by linear theory. See McLandress (1998) and Fritts and Alexander (2003) for reviews of gravity wave parameterization and surveys of commonly used schemes.

Since there is great uncertainty in all aspects of gravity wave modeling, parameterizations can be tuned extensively in order to produce a realistic forcing on the circulation. Ultimately, in order for progress to be made in parameterizing gravity-wave breaking, for example with a view to simulating future climate scenarios, it is of primary importance to understand the conditions under which a wave will break as well as the detailed dynamics of the breaking.

Mied (1976) and Drazin (1977) showed using Floquet theory that inviscid monochromatic gravity waves are linearly unstable at all amplitudes even if their amplitudes are far from the threshold for static instability and their Richardson numbers greater than 1/4, the sufficient condition for stability of a steady shear flow (Miles 1961; Howard 1961). Later, Klostermeyer

(1983) showed how weak viscosity affects the growth rates and spatial scales of the leading unstable modes, a relevant point since in the mesosphere the kinematic viscosity and thermal diffusivity are relatively large due to the very low ambient density.

The above studies neglect the effect of rotation, which becomes significant for steeply propagating waves, so-called inertia-gravity waves (IGW). Due to their very low frequencies and near horizontal symmetry, steeply propagating waves can be modeled to a large extent as steady stratified shear flows, whereby Dunkerton (1997) and Achatz and Schmitz (2006) obtained approximate analytic results. These studies and numerical studies by Yau et al. (2004), Lelong and Dunkerton (1998a,b), and Achatz (2005) found that rotation strongly affects the orientation of the most unstable perturbations relative to the propagation direction of the wave. This is because waves affected by rotation have a nonzero velocity component in the direction perpendicular to the plane of the wave. It has also been shown that shear instability occurs in IGW below the threshold for static instability.

Most numerical studies of gravity wave breaking have considered only two-dimensional breaking, but the fact that there are linearly unstable perturbations with all orientations relative to the propagation direction of the wave indicates that in practice the process must be strongly three dimensional. Nonlinear numerical simulations by Andreassen et al. (1994) (see also Fritts et al. 1994) of breaking high-frequency gravity waves found fundamentally different behaviour in two- and three-dimensional simulations, with more efficient reduction of the amplitude of the gravity wave and generation of turbulence occurring in the three-dimensional simulations. More recently, Fritts et al. (2009a,b) used simulations at much higher resolution and with higher Reynolds numbers more realistic for the atmosphere and again found differences between the two- and three-dimensional dynamics. Initially, two-dimensional structures on the scale of the initial wave dominate, while later on, local instabilities lead to the formation of small scale three-dimensional structures. Another important point is that waves with amplitudes both above and below the threshold for static instability break, but the relative sizes of the buoyancy and momentum flux differ depending

on the static stability of the wave.

There have been to our knowledge no three-dimensional direct numerical simulations (DNS), comparable to those of Fritts et al. (2009a,b), of breaking IGW (meaning waves affected by rotation) with parameters realistic for the middle atmosphere and of high enough resolution to reliably represent the small scales that emerge in the turbulent evolution of the breaking wave. This is partly because of their very long horizontal scale, a difficulty that may be overcome by a change of reference frame (as explained below) or by artificially reducing the ratio N/f (Lelong and Dunkerton 1998a,b), and partly due to the fact that since the vertical momentum flux associated with a gravity wave decreases with decreasing intrinsic frequency (Fritts et al. 2006) there has been less interest in IGW breaking than in the breaking of high frequency waves. That is not to say, however, that the cumulative effect of IGW on the large scale circulation is negligible. A recent observational case study by Nicolls et al. (2010) found that a breaking IGW with properties similar to those considered here accelerated the background flow by 10-20 ms^{-1}.

Three-dimensional simulations are of course computationally expensive, especially given the scales of low-frequency inertia-gravity waves, and are thus impractical for investigating much of parameter space. However, since for related problems three-dimensional simulations have indicated essential differences in the two- and three-dimensional aspects of wave breaking, including different temporal and spatial scales, the following three-stage approach presents itself. First, the leading primary linear instabilities of the IGW are computed. Next, high resolution nonlinear two-dimensional simulations initialized with the superposition of the IGW and its leading linear modes are performed. Finally the linear stability, with respect to perturbations varying in the remaining spatial direction, of the two-dimensional time dependent states obtained from the nonlinear integrations is considered. The latter is a two-dimensional problem because the coefficients in the linearized equations depend only on two spatial dimensions, and is the subject of the present article.

The idea of analyzing the linear stability of numerically calculated two-dimensional non-

linear solutions to perturbations varying in the perpendicular direction was used by Klaassen and Peltier (1985a,b) for the problem of Kelvin-Helmholtz instability. Assuming the growth of the secondary instabilities is much faster than the evolution of the two-dimensional basic state, they took the two-dimensional state to be time-independent. The resulting linearized equations could then be analyzed in terms of normal modes. The effect of the temporal evolution of the basic state was considered by performing the linearization at different times. Here we investigate secondary instabilities using singular vector analysis (Farrell and Ioannou 1996a,b), whereby the perturbations whose energy grows by the largest factor within a given optimization time are computed. Unlike normal mode analysis, singular vectors may be computed even for time dependent basic states. In addition, even when the system is non-normal, singular vectors are the eigenvectors of a real, symmetric matrix and thus form an orthogonal set, both at the initial time and at the optimization time, making it possible to project an arbitrary state onto a subset of the leading singular vectors without computing the whole set. Disadvantages of singular vector analysis are that the singular vectors have time dependent spatial structure and are thus difficult to compare to, say, observed structures (although it can identify temporal and spatial scales which one may compare with observations) and that it cannot distinguish between true linearly unstable, exponentially growing modes, and the transient growth of a linear combination of oscillatory modes. On the other hand, with respect to the latter point, if perturbations are finite amplitude, modes with large transient growth can be the most interesting in practice, leading to nonlinear effects which dominate the subsequent evolution.

The determination of the primary linear instabilities and the nonlinear two-dimensional integrations are the subjects of Achatz and Schmitz (2006) and Achatz (2007) respectively. To describe the orientation of the primary perturbations, we adopt the terminology of Dunkerton (1997): perturbations varying in the direction perpendicular to the plane of the wave are called *transverse*, and perturbations varying in the plane of the wave are called *parallel*. In the present article we focus on two cases identified by Achatz (2007) as particularly

effective in reducing the amplitude of the initial IGW. In both cases the wave propagates in the x-z plane with an angle of phase propagation of 89.5° to the horizontal and a vertical wavelength of 6 km. In the first case the IGW is statically unstable, with amplitude 1.2 times the threshold amplitude for static instability, and the primary perturbation is the leading transverse normal mode (varying in the y direction). The second case is a statically stable wave with non-dimensional amplitude 0.86 perturbed by a leading transverse singular vector. We also investigate the secondary instabilities of the statically unstable IGW perturbed by its leading parallel normal mode, which is the fast growing of all the normal modes.

The paper is organized as follows: In section 2, the Boussinesq equations in a coordinate system moving with the wave and rotated so that one axis is parallel to the wavevector of the IGW, as well as the properties of the IGW solution itself, are reviewed and the hierarchy of IGW, primary perturbations and secondary perturbations introduced. Section 3 is a brief outline of singular vector analysis. Section 4 describes the primary instabilities of the IGW and the basic states taken from Achatz (2007), and Section 5 discusses the secondary instabilities in terms of singular vectors.

2. Governing equations, the inertia-gravity wave solution, and primary and secondary perturbations

We use the Boussinesq equations on an f plane,

$$\frac{Du}{Dt} - fv + \frac{\partial P}{\partial x} = \nu\nabla^2 u, \tag{1a}$$

$$\frac{Dv}{Dt} + fu + \frac{\partial P}{\partial y} = \nu\nabla^2 v, \tag{1b}$$

$$\frac{Dw}{Dt} - b + \frac{\partial P}{\partial z} = \nu\nabla^2 w, \tag{1c}$$

$$\frac{Db}{Dt} + N^2 w = \mu\nabla^2 b, \tag{1d}$$

$$\frac{\partial u}{\partial x} + \frac{\partial v}{\partial y} + \frac{\partial w}{\partial z} = 0, \tag{1e}$$

where $\boldsymbol{v} = (u, v, w)$ is the velocity field, buoyancy b is defined in terms of potential temperature θ by $b \equiv (\theta - \overline{\theta})/\theta_0$, where $\overline{\theta}(z)$ is the background potential temperature and θ_0 a representative constant value, $N^2 \equiv (g/\theta_0)\mathrm{d}\overline{\theta}/\mathrm{d}z$ is the square of the Brunt-Väisälä frequency, $f \equiv 2\Omega \sin\phi_0$ is the Coriolis parameter at a reference latitude ϕ_0, ν is the kinematic viscosity, and μ the thermal diffusivity. In all simulations, a value of 1 $\mathrm{m}^2\ \mathrm{s}^{-1}$, typical of the mesopause region, was used for both ν and μ, N was constant and equal to $2 \times 10^{-2}\ \mathrm{s}^{-1}$, and the f-plane was centred at $\phi_0 = 70\mathrm{N}$. The material time derivative is defined by

$$\frac{D}{Dt} \equiv \frac{\partial}{\partial t} + \boldsymbol{v} \cdot \nabla. \tag{2}$$

In the absence of dissipation ($\nu = \mu = 0$)[1], a monochromatic inertia-gravity wave is an exact solution to (1) of the form

$$[u, v, w, b] = \mathrm{Re}\left\{[\hat{u}, \hat{v}, \hat{w}, \hat{b}] \exp\left[i(kx + mz - \omega t)\right]\right\}, \tag{3}$$

where hatted variables are complex constants, and the constants k and m are the horizontal and vertical wavenumbers, related to the frequency ω through the dispersion relation

$$\omega^2 = N^2 \cos^2\Theta + f^2 \sin^2\Theta, \tag{4}$$

where $\Theta = \tan^{-1}(m/k)$ is the angle of phase propagation of the wave relative to the horizontal. Since f and N do not depend on horizontal position, there is no preferred horizontal direction and no loss of generality in considering a wave with wavevector in the x-z plane.

The complex amplitudes satisfy the polarization relations

$$[\hat{u}, \hat{v}, \hat{w}, \hat{b}] = a\left[\frac{\omega}{k}, -i\frac{f}{k}, -\frac{\omega}{m}, i\frac{N^2}{m}\right], \tag{5}$$

where a is a dimensionless constant defined so that $a = 1$ corresponds to a wave neutral with respect to static stability at its least stable point. Notice that because of the Coriolis force, the horizontal component of the velocity vector rotates with time.

[1] In the dissipative case, if $\mu = \nu$ (Prandtl number unity), then (3) is still a solution, but with amplitude decaying with time.

As mentioned, the problem of gravity wave stability is greatly simplified by working in a Cartesian coordinate system rotated about the y axis so that the vertical axis is parallel to the wave-vector of the wave (Mied 1976). Let the new coordinates be (ξ, y, ζ), where

$$\xi = \sin\Theta\ x - \cos\Theta\ z, \tag{6a}$$

$$\zeta = \cos\Theta\ x + \sin\Theta\ z, \tag{6b}$$

with associated velocity components u_ξ, v and w_ζ.

Written in terms of ξ, y, ϕ and t, where $\phi = K\zeta - \omega t$ is the phase of the wave and $K \equiv \sqrt{k^2 + m^2}$, the system (1) becomes

$$\frac{Du_\xi}{Dt} - f\sin\Theta\ v + \frac{\partial p}{\partial \xi} + \cos\Theta\ b = \nu\nabla^2 u_\xi, \tag{7a}$$

$$\frac{Dv}{Dt} + f(\sin\Theta\ u_\xi + \cos\Theta\ w_\zeta) + \frac{\partial p}{\partial y} = \nu\nabla^2 v, \tag{7b}$$

$$\frac{Dw_\zeta}{Dt} - f\cos\Theta\ v + K\frac{\partial p}{\partial \phi} - \sin\Theta\ b = \nu\nabla^2 w_\zeta, \tag{7c}$$

$$\frac{Db}{Dt} + N^2(-\cos\Theta\ u_\xi + \sin\Theta\ w_\zeta) = \mu\nabla^2 b, \tag{7d}$$

$$\frac{\partial u_\xi}{\partial \xi} + \frac{\partial v}{\partial y} + K\frac{\partial w_\zeta}{\partial \phi} = 0, \tag{7e}$$

where now

$$\frac{D}{Dt} \equiv \frac{\partial}{\partial t} + u_\xi\frac{\partial}{\partial \xi} + v\frac{\partial}{\partial y} + (Kw_\zeta - \omega)\frac{\partial}{\partial \phi}, \tag{8}$$

and the gravity wave solution (3) becomes

$$u_\xi = U_\xi^{(0)} = -\frac{\sqrt{K^2}\omega}{km}\sin\phi, \tag{9a}$$

$$v = V^{(0)} = \frac{f}{k}\cos\phi, \tag{9b}$$

$$w_\zeta = W_\zeta^{(0)} = 0, \tag{9c}$$

$$b = B^{(0)} = -\frac{N^2}{m}\cos\phi. \tag{9d}$$

Using ϕ as coordinate in place of ζ places us in the reference frame moving with the phase velocity of the gravity wave.

The instability analysis proceeds by linearizing (7) about the solution (9) and looking for growing perturbations. Because the gravity wave is independent of ξ and y, perturbation solutions exist of the form

$$[u_\xi^{\prime(p)}, v^{\prime(p)}, w_\zeta^{\prime(p)}, b^{\prime(p)}] = \mathrm{Re}\left\{[\hat{u}_\xi^{\prime(p)}(\phi,t), \hat{v}^{\prime(p)}(\phi,t), \hat{w}_\zeta^{\prime(p)}(\phi,t), \hat{b}^{\prime(p)}(\phi,t)] \exp\left[i(k_\xi \xi + k_y y)\right]\right\}, \tag{10}$$

which we refer to as *primary perturbations*. While it may be unstable to three-dimensional perturbations, if not perturbed a nonlinear integration initialized with an IGW and one of its leading unstable primary perturbations remains two-dimensional in space, with all fields depending on only the IGW phase ϕ and the spatial coordinate in the direction of the wavevector (k_ξ, k_y) of the primary perturbation. It is therefore convenient to introduce an additional coordinate transformation

$$x_\parallel = \cos\alpha\ \xi + \sin\alpha\ y, \tag{11a}$$

$$y_\perp = -\sin\alpha\ \xi + \cos\alpha\ y, \tag{11b}$$

where $\alpha \equiv tan^{-1}(k_y/k_\xi)$, and the corresponding velocity components $u_\parallel$ and $v_\perp$. For parallel primary perturbations $u_\parallel = u_\xi$ and $v_\perp = v$, and for transverse primary perturbations $u_\parallel = v$ and $v_\perp = -u_\xi$.

We investigate the three-dimensionalization of the turbulence that develops in the breaking of an inertia-gravity wave by linearizing (7) about the time-dependent nonlinear development of the state initialized with the IGW and a leading primary perturbation, referred to henceforth as the time-dependent *basic state*,

$$[u_\parallel, v_\perp, w_\varsigma, b] = \left[U_\parallel(x_\parallel,\phi,t), V_\perp(x_\parallel,\phi,t), W_\varsigma(x_\parallel,\phi,t), B(x_\parallel,\phi,t)\right], \tag{12}$$

yielding

$$\frac{D'u'_\parallel}{Dt} + \frac{\partial U_\parallel}{\partial x_\parallel}u'_\parallel + K\frac{\partial U_\parallel}{\partial \phi}w'_\zeta - f(\sin\Theta\ v'_\perp + \sin\alpha\cos\Theta\ u'_\parallel) + \frac{\partial p'}{\partial x_\parallel} + \cos\alpha\cos\Theta\ b' = \nu\nabla^2 u'_\parallel, \tag{13a}$$

$$\frac{D'v'_\perp}{Dt} + \frac{\partial V_\perp}{\partial x_\parallel}u'_\parallel + K\frac{\partial V_\perp}{\partial \phi}w'_\zeta + f(\sin\Theta\ u'_\parallel + \cos\alpha\cos\Theta\ w'_\zeta) + \frac{\partial p'}{\partial y_\perp} - \sin\alpha\cos\Theta\ b' = \nu\nabla^2 v'_\perp, \tag{13b}$$

$$\frac{D'w'_\zeta}{Dt} + \frac{\partial W_\zeta}{\partial x_\parallel}u'_\parallel + K\frac{\partial W_\zeta}{\partial \phi}w'_\zeta - f(\sin\alpha\cos\Theta\ u'_\parallel + \cos\alpha\cos\Theta\ v'_\perp) + K\frac{\partial p'}{\partial \phi} - \sin\Theta\ b' = \nu\nabla^2 w'_\zeta, \tag{13c}$$

$$\frac{D'b'}{Dt} + N^2(-\cos\alpha\cos\Theta\ u'_\parallel + \sin\alpha\cos\Theta\ v'_\perp + \sin\Theta\ w'_\zeta) = \mu\nabla^2 b', \tag{13d}$$

$$\frac{\partial u'_\parallel}{\partial x_\parallel} + \frac{\partial v'_\perp}{\partial y_\perp} + K\frac{\partial w'_\zeta}{\partial \phi} = 0, \tag{13e}$$

where

$$\frac{D'}{Dt} \equiv \frac{\partial}{\partial t} + U_\parallel\frac{\partial}{\partial x_\parallel} + V_\perp\frac{\partial}{\partial y_\perp} + (KW_\zeta - \omega)\frac{\partial}{\partial \phi}. \tag{14}$$

Since the coefficients in (13) are independent of $y_\perp$, we may seek solutions of the form

$$[u'_\parallel, v'_\perp, w'_\zeta, b'] = \mathrm{Re}\left\{[\hat{u}'_\parallel(x_\parallel,\phi,t), \hat{v}'_\perp(x_\parallel,\phi,t), \hat{w}'_\zeta(x_\parallel,\phi,t), \hat{b}'(x_\parallel,\phi,t)]\exp(ik_\perp y_\perp)\right\}, \tag{15}$$

which we call *secondary perturbations*. The perturbation pressure p' is found by solving a Poisson equation obtained by demanding that the perturbation velocity field remain nondivergent.

Note that as much as possible, results will be given in terms of coordinates (ξ, y, ζ) and dependent variables (u_ξ, v, w_ζ, b) in the IGW frame to facilitate comparisons between parallel and transverse perturbations and between primary and secondary instabilities.

Energy Budget

The size of perturbations is measured in terms of the change in the perturbation total energy

$$E' = \frac{1}{K} \iiint \left[\frac{1}{2} \left(u_{\parallel}'^2 + v_{\perp}'^2 + w_{\zeta}'^2 + \frac{b'^2}{N^2} \right) \right] dx_{\parallel} dy_{\perp} d\phi, \tag{16}$$

where the integration is over one wavelength of each of the IGW and the primary and secondary perturbations. E' grows or decays through interaction between the perturbation and the basic state and decays through dissipation. By analyzing the various momentum and buoyancy flux terms in the time derivative of E',

$$\begin{aligned} \frac{dE'}{dt} = \frac{1}{K} \iiint \Bigg[& -u_{\parallel}'^2 \frac{\partial U_{\parallel}}{\partial x_{\parallel}} - K u_{\parallel}' w_{\zeta}' \frac{\partial U_{\parallel}}{\partial \phi} - v_{\perp}' u_{\parallel}' \frac{\partial V_{\perp}}{\partial x_{\parallel}} - K v_{\perp}' w_{\zeta}' \frac{\partial V_{\perp}}{\partial \phi} \\ & - w_{\zeta}' u_{\parallel}' \frac{\partial W_{\zeta}}{\partial x_{\parallel}} - K w_{\zeta}'^2 \frac{\partial W_{\zeta}}{\partial \phi} - \frac{1}{N^2} b' u_{\parallel}' \frac{\partial B}{\partial x_{\parallel}} - \frac{K}{N^2} b' w_{\zeta}' \frac{\partial B}{\partial \phi} \\ & - \nu \left(\left| \nabla u_{\parallel}' \right|^2 + \left| \nabla v_{\perp}' \right|^2 + \left| \nabla w_{\zeta}' \right|^2 \right) - \frac{\mu}{N^2} \left| \nabla b' \right|^2 \Bigg] dx_{\parallel} dy_{\perp} d\phi, \end{aligned} \tag{17}$$

as functions of time, the mechanisms responsible for perturbation growth may be inferred. Typically, since the gravity wave is statically unstable or near the static stability threshold, the terms in (17) involving components of the buoyancy gradient are important at early times. However, at later times, the shear in the basic-state velocity field often plays a role. By analogy with growth of sinusoidally varying perturbations in the presence of vertical velocity shear, we call growth due to shear in $U_{\parallel}$ (the basic state velocity component transverse to the direction of sinusoidal variation of the secondary perturbation), a generalized *roll mechanism*, and growth due to shear in $V_{\perp}$ a generalized *Orr mechanism*. See Achatz and Schmitz (2006) and Bakas et al. (2001) for discussions of the roll and Orr mechanisms for perturbation growth in the presence of vertical velocity shear.

Numerical models

All numerical integrations, including the two-dimensional nonlinear simulations for determining the basic states and the linear integrations required for determining the primary

and secondary perturbations, are performed with the numerical models developed by Achatz (2005, 2007).

As described in Achatz (2005), primary perturbations in the form of normal modes are computed using a one-dimensional linear model constructed by linearizing (7) about (9) and substituting (10) for the perturbation fields. The independent variables are the real and imaginary parts of $\hat{u}_\xi^{\prime(p)}(\phi,t)$, $\hat{v}^{\prime(p)}(\phi,t)$, $\hat{w}_\zeta^{\prime(p)}(\phi,t)$, and $\hat{b}^{\prime(p)}(\phi,t)$ evaluated on the discretized ϕ axis. Singular vectors additionally require the corresponding adjoint model, which was developed using the utility TAMC (Giering and Kaminski 1998).

The nonlinear integrations used for generating the basic states are performed at high enough resolution to resolve scales down to close to the Kolmogorov scale of three-dimensional turbulence, here a few metres. Note that while the model is two dimensional in space, the velocity field is three dimensional, and crucially, the vortex tube tilting mechanism is active. As a result, the turbulence that develops is more like three-dimensional turbulence, with a direct cascade of energy to small scales, than it is like two-dimensional turbulence with its inverse cascade. Such a model is therefore sometimes referred to as 2.5D (Achatz 2007).

The secondary singular vectors are computed using a two-dimensional model to solve the system (13) with solutions of the form (15) inserted. The dependent variables are the real and imaginary parts of $\hat{u}'_\parallel(x_\parallel,\phi,t)$, $\hat{v}'_\perp(x_\parallel,\phi,t)$, $\hat{w}'_\zeta(x_\parallel,\phi,t)$, and $\hat{b}'(x_\parallel,\phi,t)$ evaluated on the discrete $x_\parallel$-ϕ grid. Again, the corresponding adjoint model required for finding singular vectors was developed with the help of TAMC.

For all models, the spatial discretization is a staggered one- or two-dimensional C grid (see, for example, Durran 1999) and the time stepping is performed using a third-order-accurate Runge-Kutta method. Eigenvalues are computed iteratively using a variant of the Arnoldi process with the FORTRAN library ARPACK (Lehoucq et al. 1998).

3. Singular vectors

Singular vector analysis (Farrell and Ioannou 1996a,b) of a linear system finds the perturbations whose energy (or another norm) grows by the largest factor in a given optimization time. Consider a discrete system of the form

$$\frac{\mathrm{d}\mathbf{x}}{\mathrm{d}t} = \mathbf{A}\mathbf{x}, \tag{18}$$

where $\mathbf{x}$ is a vector and $\mathbf{A}$ is a real, possibly time dependent matrix, and introduce a norm

$$||\mathbf{x}||^2 \equiv \mathbf{x}^T\mathbf{M}\mathbf{x}. \tag{19}$$

Then, given an optimization time τ, define the propagator matrix $\mathbf{\Phi}(\tau)$ such that

$$\mathbf{x}(\tau) = \mathbf{\Phi}(\tau)\mathbf{x}(0). \tag{20}$$

It can be shown that the initial perturbation $\mathbf{x}(0)$ that maximizes the growth factor

$$\sigma \equiv \frac{||\mathbf{x}(\tau)||}{||\mathbf{x}(0)||} \tag{21}$$

is the leading eigenvector of the matrix $\mathbf{M}^{-1}\overline{\mathbf{\Phi}}^T(\tau)\mathbf{M}\mathbf{\Phi}(\tau)$. It can furthermore be shown that the eigenvectors $\{\mathbf{p}_k\}$ of the matrix, called singular vectors, are mutually orthogonal with respect to the inner product induced by $\mathbf{M}$, as are the vectors $\{\mathbf{\Phi}(\tau)\mathbf{p}_k\}$. Note that since the propagator matrix $\mathbf{\Phi}(\tau)$ is never calculated explicitly, the appearance of the adjoint matrix $\overline{\mathbf{\Phi}}(\tau)^T$ means that in practice the adjoint model corresponding to the discrete tangent linear model must be developed.

If $\mathbf{A}$ is independent of time, as is the case for the primary instability problem, the normal modes of (18) may be computed. The spatial structure of the normal modes is given by the eigenvectors of $\mathbf{A}$, and the real parts of the corresponding complex eigenvalues represent the growth or decay rates. Since computing the full set of normal modes involves finding the eigenvectors of a very large matrix, and since we are interested in only the normal modes with largest growth rates, it is advantageous to work with the matrix $\exp(\tau\mathbf{A})$, obtained

approximately by integrating the linear system (18) for some finite time τ. Its eigenvectors are the same as those of $\mathbf{A}$, and its complex eigenvalues are of the form $\Lambda = e^{\lambda_r t} e^{i\lambda_i t}$, where $\lambda_r + i\lambda_i$ is an eigenvalue of $\mathbf{A}$. The Arnoldi iteration is used to find the eigenvalues Λ with the largest square moduli, which correspond to the growth factors of the leading normal modes after time τ.

Since the inertia-gravity wave is independent of time in the rotated and co-moving reference frame, the primary perturbations can be either singular vectors or normal modes, depending on the application. However, since the basic state for secondary perturbations is time-dependent, of the two, only singular vector analysis may be applied.

4. Primary instabilities

Achatz (2005) calculated the leading normal modes and singular vectors for a wide range of IGW parameter choices, from which Achatz (2007) identified a few cases in which initial perturbations lead to significant decay of the original wave in corresponding nonlinear simulations. We focus here on the case of an IGW with wavelength 6 km and propagation angle 89.5° to the horizontal, propagating on an f-plane centred at latitude 70 N, and consider both a statically unstable wave, with nondimensional amplitude $a = 1.2$ (zonal velocity amplitude of 29 m s^{-1}), and a statically and dynamically stable wave, with nondimensional amplitude $a = 0.86$ (zonal velocity amplitude of 21 m s^{-1}). The waves have a period of approximately 8 hours.

The leading perturbations all have energy initially concentrated near the level of minimum static stability, i.e. where $\partial B^{(0)}/\partial z$ is most negative, which is located near $\phi = 3\pi/2$ for the IGW solution (9). At the same level, there is maximum vertical shear in the transverse velocity component $V^{(0)}$ and the parallel velocity component $U_\xi^{(0)}$ has a local minimum. The regions with vertical shear in $U_\xi^{(0)}$ are located one quarter wavelength above and below the level of minimum static stability.

For the statically unstable wave, Achatz (2007) found that in nonlinear simulations, perturbation of the IGW by its leading normal mode was more effective in initiating wave breaking than perturbation by its leading singular vector. The left panel of Fig. 1 shows the growth factor after 5 minutes as a function of wavelength in the ξ-y plane for the limiting cases of parallel perturbations ($k_y = 0$), where the perturbation varies in the ξ direction, and transverse perturbations ($k_\xi = 0$), where the perturbation varies in the y direction.

While short wavelength parallel perturbations have the larger growth factors, long wavelength transverse perturbations lead to more dissipation of the original inertia-gravity wave (see Fig. 4 of Achatz 2007). An interpretation of this is that the shorter wavelength structures also have shorter scale in the phase direction, which leads to the formation of strong gradients, an earlier onset of Kelvin-Helmholtz type instabilities, and relatively rapid nonlinear saturation of the initial instability. Slower developing, larger scale structures (with correspondingly weaker gradients) that propagate in the phase direction can draw energy from the shear in all parts of the wave, initially through buoyancy conversion and the generalized Orr mechanism, and later through the more efficient generalized roll mechanism as the perturbation propagates away from the level of minimum static stability toward regions of shear in U_ξ.

Here we therefore focus on the case where the leading transverse normal mode, which has a wavelength λ_y of 7.943 km, is the initial perturbation to the statically unstable IGW. The two-dimensional nonlinear model was run in a 7.943 km $\times$ 6 km doubly periodic rectangular domain with 1152 points in each of the y and ζ directions (noting that the model uses $\phi \in [0, 2\pi]$ as vertical coordinate) for a spatial resolution of about 6 m. The initial amplitude of the normal mode was such that the maximum perturbation energy density was 5% of the energy density of the IGW, the latter being uniform in space. This choice was large enough that nonlinear effects become significant and small enough that the flow has not yet become turbulent before the five minute optimization time of the secondary singular vector calculation has passed. Fig. 2 shows the basic state B, U_ξ and V fields at the initial time,

after 5 minutes (the optimization time for the secondary singular vector calculations), and after 20 minutes.

For completeness, we also investigated the leading parallel normal mode, which has a wavelength λ_ξ of 501 m. The nonlinear model was run with 2304 points in the ζ direction and 288 in the ξ direction. As was found by Achatz (2007), perturbation growth in the 2.5D simulations is dominated by the transverse component of velocity, V, shown in Fig. 3 at the initial time, after 3 minutes and after 20 minutes. Notice that the perturbation remains much more localized near $\phi = 3\pi/2$ than in the transverse normal mode case (Fig. 2). For the secondary singular vector calculation, a short optimization time of 3 minutes was chosen because the basic state fields become filamented and then turbulent earlier than in the case with a transverse primary perturbation.

Achatz (2005) showed numerically that no exponentially growing normal modes exist for the statically stable IGW considered here (its amplitude is such that the Richardson number is slightly greater than 1/4), but that the leading singular vectors were nevertheless effective in leading to breaking of the original wave. The right panel of Fig. 1 shows the growth factor after an optimization time of 5 minutes as a function of horizontal wavelength in the ξ-y plane for the leading parallel and transverse singular vectors. As in the case of the statically unstable IGW, nonlinear simulations show that the longer-wavelength leading transverse perturbations lead to more effective breaking than the faster growing shorter wavelength parallel perturbations. We therefore use the leading transverse singular vector, with a wavelength $\lambda_y = 3.162$ km, as the initial perturbation for the basic state. Since the spatial structure of the singular vector changes with time, the initial amplitude of the singular vector is especially significant, affecting the spatial structure of the fields as nonlinear effects become important. We chose an initial amplitude of the perturbation to be such that the maximum perturbation energy density is 10% of the energy density in the IGW. For these simulations, we again used a rectangular domain with sides equal to the wavelengths of the primary perturbation and the IGW, 3.162 km in the y direction and 6 km in the ζ direction,

with, respectively, 1152 points and 2304 points for a spatial resolution of approximately 3 m. Fig. 4 shows the basic state fields at the initial time, after 5 minutes, and after 20 minutes.

5. Secondary instabilities

The secondary instability analysis proceeds as follows: The Boussinesq equations (7) are linearized about one of the time dependent basic states described above, i.e. the nonlinear two-dimensional simulations initialized with either a statically unstable IGW perturbed by its leading parallel or transverse normal mode or a statically stable IGW perturbed by its leading transverse singular vector. A solution of the form (15) is substituted into the resulting linearized equations (13), yielding a set of partial differential equations for the complex amplitudes $\hat{u}'_{\parallel}$, $\hat{v}'_{\perp}$, $\hat{w}'_{\zeta}$, and $\hat{b}'$ with coefficients periodic in the $x_{\parallel}$ and ϕ directions and in which the wavelength of the perturbation in the $y_{\perp}$ direction, $\lambda_{\perp} = 2\pi/k_{\perp}$, is a parameter.

The secondary instabilities in which we are interested are of larger scale than the 3 m to 6 m scale resolved by the nonlinear simulations, and the hundreds of integrations necessary to determine the leading singular vectors at such high resolution would be prohibitively expensive in terms of computing resources. We found that a grid of 128 $\times$ 512 points (a resolution of 25-50 m in the y direction and the equivalent of 10 m in the ϕ direction) was sufficient for the two cases with transverse primary perturbations, the higher resolution in the ϕ direction required because the gradients in the basic state are predominantly in the ϕ direction. For the statically unstable IGW perturbed by its leading parallel normal mode, the same 128 $\times$ 512 grid was used, representing a more isotropic resolution of 5 to 10 m in both the ξ and ϕ directions.

Due to the symmetry of the system, for finite $\lambda_{\perp}$, the singular vectors come in pairs with identical growth factors and spatial structures, corresponding to phase shifts of $\pi/2$ in all variables. We will not distinguish between degenerate singular vectors and by the terms *lead-*

ing, *second-leading*, and *trailing* singular vectors, refer to non-degenerate perturbations. The mode with $k_\perp = 0$ (i.e. $\lambda_\perp = \infty$) is not degenerate, and may be thought of as a modification of the primary instability due to the nonlinear evolution of the primary perturbation.

We consider the cases of the statically unstable and statically stable IGW separately in terms of the growth factors and spatial structure of the leading singular vectors and the dominant energy conversion mechanisms. The singular vectors are then compared to integrations of the linear model initialized with a random perturbation with $|\boldsymbol{k}|^{-5/3}$ energy density spectrum, where $\boldsymbol{k}$ is the perturbation wavevector in the $x_\parallel$-ζ plane, corresponding to an isotropic three-dimensional turbulent flow.

a. Statically unstable IGW and transverse primary NM

We begin with the case of the statically unstable IGW perturbed by its leading transverse normal mode (cf. Fig. 2). For transverse primary perturbations, $y_\perp = -\xi$ and $\lambda_\perp = \lambda_\xi$. Fig. 5 shows growth factors for the leading singular vectors plotted against λ_ξ. The growth factor of the leading singular vector is indicated by the solid curve and of the second leading singular vector by the dashed curve. The single largest growth factor occurs for $\lambda_\xi = 150$ m, but there is a second peak in the growth factor curve of the second leading singular vector at a wavelength of about 800 m. At each of the two peaks, the 20 leading singular vectors were computed and their growth factors are indicated by filled diamonds. Shown in the right panel of the figure are the growth factors of the ensemble of initially random perturbations. The growth factors of the randomly initialized integrations are naturally much smaller than those of the singular vectors, the latter being optimally initialized to maximize the growth factor. One notices again two peaks, one near $\lambda_\xi = 215$ m, and the other near $\lambda_\xi = 800$ m. Here, the longer wavelength peak is higher than the shorter wavelength peak. This might be explained by the fact that for $\lambda_\xi = 800$ m, the growth factors of the leading singular vectors are closer together, while at the $\lambda_\xi = 150$ m peak, the growth factor decreases quickly after the leading singular vector. The random initializations at $\lambda_\xi = 800$ m therefore project onto

more singular vectors with significant growth factors.

Fig. 6 shows contours of perturbation vertical velocity amplitude $\hat{w}'_\zeta$ corresponding to the leading singular vector at $\lambda_\xi = 150$ m plotted over the basic state buoyancy field at the initial time, halfway to the optimization time, and at the optimization time. Notice how the time dependent structure of the singular vector follows the location of maximum negative vertical buoyancy gradient.

For the leading few singular vectors at each of the peaks in the growth factor curve and for the randomly initialized integrations at the same values of λ_ξ, the integrated energy conversion rate densities decomposed into contributions from the shears in each velocity component and from the buoyancy gradient (see Eq. 17) are plotted as functions of time in Fig. 7. The contributions due to gradients of B represent buoyancy conversion, and the contributions due to shear in U_ξ and V represent growth through the generalized Orr and roll mechanisms respectively. The linear model is integrated past the optimization time to see how robust the growth captured by the singular vectors is. All curves are normalized by the total perturbation energy at each time and can be interpreted as instantaneous effective growth rates. The energy conversion rates of the leading singular vector match qualitatively with the corresponding curves for the random initialzations. The dominant growth mechanism is buoyancy conversion throughout, with a late contribution from the roll mechanism (growth due to shear in V). This is consistent with the earlier noted observation that the energy in the singular vector is concentrated near the location of maximum negative buoyancy gradient. The randomly initialized integrations take time to become organized but the energy conversion rate curves match those of the singular vector close to and beyond the optimization time. The small variation in the conversion curves for the random ensemble, indicated by error bars, and their resemblance to those of the singular vector suggest that the dynamics of the singular vectors is representative of the instability of the basic state.

For $\lambda_\xi = 800$ m the picture is somewhat different. In this case the second-leading and trailing singular vectors (not shown for trailing singular vectors) more closely resemble

the random ensemble than does the leading singular vector (see Fig. 8). While buoyancy conversion is the most important mechanism at early times, nearer the optimization time growth due to shear in U_ξ takes over. Contours of perturbation vertical velocity are shown in Fig. 9 over contours of basic state U_ξ at the initial time, at half the optimization time, and at the optimization time for both the second leading singular vector and for one of the randomly initialized integrations. The structures in the singular vector perturbation field are larger scale in y and ζ than their counterparts in the $\lambda_\xi = 150$ m case (Fig. 6). This isotropic scaling (here the scales in all three directions are on the order of 1 km) seems to be a generic phenomenon: growing perturbations of larger scale in the ξ direction also have larger scales in the y and ζ directions. Also, the initial concentration of perturbation energy in the singular vector does not coincide with a region of strong gradient in U_ξ, but it does in the later snapshots. This is consistent with the energy conversion rates plotted in Fig. 8, where growth due to shear in U_ξ becomes important only at later times. The final state of the randomly initialized integration qualitatively resembles that of the singular vector.

b. Statically unstable IGW and parallel primary NM

For the case of the statically unstable IGW perturbed by its leading parallel normal mode (cf. Fig. 3), $x_\parallel = \xi$ and $\lambda_\perp = \lambda_y$. Fig. 10 shows the growth factors after three minutes of secondary perturbations as functions of λ_y for the leading singular vectors and an ensemble of randomly initialized integrations. There is very close agreement in terms of the position of the peak and the shape of the growth factor curves, probably because the leading singular vector is so dominant. The spatial structures of the $\hat{u}'_\xi$, $\hat{v}'$, and $\hat{w}'_\zeta$ components of the leading singular vector with $\lambda_y = 270$ m are shown in Fig. 11. The perturbations are aligned with the region of strongest gradient in the basic state V field, again consistent with the energy conversion rates (Fig. 12), which are dominated by terms proportional to the gradient of V.

Note that while the secondary instabilities of the IGW perturbed by its leading transverse NM resemble the parallel primary instabilities in terms of length scale and growth mecha-

nism, in this case the filamentation that occurs due to the rapid growth of the small-scale primary perturbation leads to shear instabilities before the large-scale transverse perturbations can grow through the Orr mechanism associated with vertical shear in U_ξ. The small-scale primary and secondary instabilities will, inevitably, saturate rapidly in nonlinear three-dimensional simulations and are probably not as relevant as the transverse primary perturbations which lead to more significant dissipation of the original wave.

c. Statically stable IGW and transverse primary SV

The results for the secondary instabilities of the statically stable IGW are somewhat less clear, but we can still draw conclusions in terms of scales and growth mechanisms like we did in the case of the statically unstable wave.

Growth factors for the leading secondary singular vectors plotted against λ_ξ for the statically stable wave are shown in Fig. 13, along with the corresponding growth factor curves for an ensemble of randomly initialized integrations. There is a single peak near $\lambda_\xi = 485$ m, but the largest growth factors occur for $\lambda_\xi = \infty$. The growth factors of the leading 20 singular vectors at $\lambda_\xi = 485$ m are indicated by the filled diamonds, and at $\lambda_\xi = \infty$ by the horizontal line segments at the right edge of the figure. The growth factor curves for the ensemble of randomly initialized runs do not show a single clear peak, although individual cases (each curve represents the same initial distribution in y and ϕ but with a different value of λ_ξ) have local maxima at $\lambda_\xi < 1$ km, and, like the leading singular vector curve, tend to increase as λ_ξ becomes very large.

The energy conversion rates as functions of time are shown in Fig. 14 for the leading singular vectors and randomly initialized integrations for both $\lambda_\xi = 485$ m and $\lambda_\xi = \infty$. As in the statically unstable IGW case, the linear integrations are extended beyond the optimization time. While the infinite wavelength runs have larger growth factors at the optimization time (5 minutes), for a longer run (10 minutes), the short wavelength runs have much higher growth factors (the growth factors are not shown, but are reflected in the

higher conversion rates past the optimization time). For $\lambda_\xi = 485$ m, the dominant energy conversion mechanism is the generalized Orr mechanism (growth due to interaction with shear in U_ξ). For $\lambda_\xi = \infty$ both buoyancy conversion and the Orr mechanism are significant. At later times, and especially beyond the optimization time, the randomly initialized runs show very similar behaviour to the leading singular vector.

For the $\lambda_\xi = 485$ m perturbations, Fig. 15 shows the energy conversion rate *densities* due to, respectively, the buoyancy gradient and shear in U_ξ and V as functions of space at the optimization time for both a randomly initialized integration and the same initial condition projected onto the leading 20 singular vectors. The spatial distribution of the energy conversion in the full field is largely represented by just the leading singular vectors. At the optimization time buoyancy conversion is no longer the dominant growth mechanism for perturbations but is in fact an energy sink. The dominant mechanism at the optimization time is the generalized Orr mechanism, and as one would expect, it acts in regions of strong gradients in U_ξ (compare with the centre panel of Fig. 4). Note that this result for the secondary singular vector might be compared with the case of the leading *parallel* primary singular vector, whose growth is dominated by buoyancy conversion and the *roll mechanism* (Achatz 2005). Evidently the effect of the transverse primary perturbation is to change the nature of the leading instability with respect to perturbations varying in the ξ (parallel) direction.

6. Summary and discussion

We have demonstrated a systematic, computationally economical method for investigating the three dimensionalization of turbulence in breaking inertia gravity waves (IGW) in the Boussinesq equations. In earlier studies, Achatz (2005; 2007) computed leading linear instabilities (normal modes and singular vectors) of IGW as functions of perturbation wavelength and orientation relative to the direction of IGW propagation and used high-resolution

"2.5D" simulations to identify the perturbations most important for wave breaking. In the present study, we have applied singular vector analysis to the equations linearized about nonlinearly evolving basic states, focusing on two cases identified by Achatz (2007) as leading to significant dissipation of the IGW in the 2.5D simulations: a statically unstable IGW perturbed by its leading transverse normal mode, and a statically stable IGW perturbed by its leading transverse singular vector.

The singular vector results suggest that the dominant spatial scales of the secondary instabilities are an order of magnitude shorter than the scales of the IGW (and of the leading tranverse primary perturbations). For the statically unstable IGW with wavelength $\lambda = 6$ km, perturbed by a transverse normal mode with wavelength $\lambda_y \approx 8$ km, the leading secondary singular vector has wavelength of just $\lambda_\xi = 150$ m. The singular vector growth factor spectrum has a second peak near $\lambda_\xi = 800$ m, and randomly initialized linear integrations suggest that the longer wavelength perturbations grow on average somewhat faster than perturbations of the shorter scale of the leading singular vector. Two important points to note are that the scale of the spatial structures of the leading secondary perturbations in the y-ζ plane is similar to the wavelength of the perturbations in the ξ direction (isotropic scaling) and that the dominant growth mechanism depends on the spatial scale – buoyancy driven production of potential energy for the short perturbations and for the longer perturbations, the generalized Orr mechanism of growth due to shear in the basic state velocity component U_ξ.

For the statically stable IGW perturbed by its leading transverse singular vector of wavelength $\lambda_y \approx 3$ km, the secondary perturbations with the largest growth after an optimization time of 5 minutes have infinite λ_ξ (i.e. they do not vary in the ξ direction), but longer integrations of the linear model show that perturbations with $\lambda_\xi = 485$ m grow significantly more.

We also consider the statically unstable IGW perturbed its leading parallel normal mode, which has the largest linear growth rate of any perturbation but appears to saturate quickly

in 2.5D simulations without leading to strong dissipation of the original wave. Like the primary perturbations, the leading secondary singular vectors in this case grow through a shear instability associated with basic state V.

A weakness of singular vector analysis as a diagnostic tool is that the spatial structures it identifies are time-dependent, so they cannot be expected to be recognized in observations. To address this point, we compared the growth factor spectra, spatial scales and growth mechanisms of the singular vectors with randomly initialized integrations of the linear model and found consistent agreement. A natural question is how much of the growth of random perturbations can be "explained" by the leading singular vectors. Since singular vectors are mutually orthogonal at both the initial and optimization times, it is a simple matter to project the state at the optimization time of the randomly initialized integrations onto a subset of the singular vectors. The energy *not* contained in the leading n singular vectors for $\lambda_\xi = 150$ m and $\lambda_\xi = 800$ m for the statically unstable IGW perturbed by its leading transverse NM and $\lambda_\xi = 485$ m for the statically stable IGW is plotted against n in Fig. 16. Between about 10% and 30% of the total perturbation energy is contained in the leading 20 singular vectors. This is considerable since the discretized system has on the order of 10^4 degrees of freedom.

Since wave-breaking is an inherently three dimensional and multi-scale phenomenon, definitive conclusions require three-dimensional nonlinear simulations with high enough resolution to resolve the small scales of turbulence and domains large enough to contain the large-scale instabilities which dominate the early phase of wave breaking. While high-resolution three-dimensional numerical simulations of breaking high frequency gravity waves have been done (Fritts et al. 2009a,b), to our knowledge no such simulations of breaking low-frequency *inertia*-gravity waves (waves affected by rotation) have yet been done. Our results suggest that the scales of the instabilities are such that the dominant structures can be contained in a domain considerably smaller than the cube of the wavelength of the IGW, and the rotated coordinate system allows for the accommodation of the very large horizontal scale

of IGW in the earth frame. Such simulations, initialized with the IGW, a leading primary perturbation, and a leading secondary singular vector, would serve as data for evaluating large eddy simulation (LES) methods as well as gravity-wave drag parameterization schemes used in climate and general circulation models.

Acknowledgments.

This work was supported by the Deutsche Forschungsgemeinschaft through the Met-Ström Priority Research Program (SPP 1276) and the grant Ac 71/4-1 and by the Leibniz-Gemeinschaft (WGL) through the PAKT program.

REFERENCES

Achatz, U., 2005: On the role of optimal perturbations in the instability of monochromatic gravity waves. *Phys. Fluids*, **17**, 1–27.

Achatz, U., 2007: The primary nonlinear dynamics of modal and nonmodal perturbations of monochromatic inertia-gravity waves. *J. Atmos. Sci.*, **64**, 74–95.

Achatz, U. and G. Schmitz, 2006: Shear and static instability of inertia-gravity wave packets: Short-term modal and nonmodal growth. *J. Atmos. Sci.*, **63**, 397–413.

Andreassen, O., C. E. Wasberg, D. C. Fritts, and J. R. Isler, 1994: Gravity wave breaking in two and three dimensions 1. Model description and comparison of two-dimensional evolutions. *J. Geophys. Res.*, **99**, 8095–8108.

Bakas, N. A., P. J. Ioannou, and G. E. Kefaliakos, 2001: The emergence of coherent structures in stratified shear flow. *J. Atmos. Sci*, **58**, 2790–2806.

Bretherton, F. P., 1966: The propagation of groups of internal gravity waves in a shear flow. *Quart. J. Roy. Met. Soc.*, **92**, 466–480.

Drazin, P. G., 1977: On the instability of an internal gravity wave. *Proc. R. Soc. London*, **356**, 411–432.

Dunkerton, T. J., 1997: Shear instability of internal inertia-gravity waves. *J. Atmos. Sci.*, **54**, 1628–1641.

Durran, D. R., 1999: *Numerical Methods for Wave Equations in Geophysical Fluid Dynamics*. Springer, New York, 465pp. pp.

Farrell, B. F. and P. J. Ioannou, 1996a: Generalized stability theory. Part I: Autonomous operators. *J. Atmos. Sci.*, **53**, 2025–2040.

Farrell, B. F. and P. J. Ioannou, 1996b: Generalized stability theory. Part II: Nonautonomous operators. *J. Atmos. Sci.*, **53**, 2041–2053.

Fritts, D. C. and M. J. Alexander, 2003: Gravity wave dynamics and effects in the middle atmosphere. *Rev. Geophys.*, **41**, 3.1–3.64.

Fritts, D. C., J. R. Isler, and O. Andreassen, 1994: Gravity wave breaking in two and three dimensions 2. Three-dimensional evolution and instability structure. *J. Geophys. Res.*, **99**, 8109–8123.

Fritts, D. C., S. L. Vadas, and J. A. Werne, 2006: Mean and variable forcing of the middle atmosphere by gravity waves. *J. Atmos. Sol.-Terr. Phys.*, **68**, 247–265.

Fritts, D. C., L. Wang, J. Werne, T. Lund, and K. Wan, 2009a: Gravity wave instability dynamics at high Reynolds numbers. Part I: Wave field evolution at large amplitudes and high frequencies. *J. Atmos. Sci.*, **66**, 1126–1148.

Fritts, D. C., L. Wang, J. Werne, T. Lund, and K. Wan, 2009b: Gravity wave instability dynamics at high Reynolds numbers. Part II: Turbulence evolution, structure, and anisotropy. *J. Atmos. Sci.*, **66**, 1149–1171.

Giering, R. and T. Kaminski, 1998: Recipes for adjoint code construction. *ACM Trans. Math. Software*, **24**, 437–474.

Grimshaw, R., 1975: Internal gravity waves: critical layer absorption in a rotating fluid. *J. Fluid Mech.*, **70**, 287–304.

Holton, J. R., 1982: The role of gravity wave induced drag and diffusion in the momentum budget of the mesosphere. *J. Atmos. Sci.*, **39**, 791–799.

Houghton, J. T., 1978: The stratosphere and the mesosphere. *Quart. J. Roy. Meteor. Soc.*, **104**, 1–29.

Howard, L. N., 1961: Note on a paper of John W. Miles. *J. Fluid Mech.*, **10**, 509–512.

Klaassen, G. P. and W. R. Peltier, 1985a: Evolution of finite amplitude Kelvin-Helmholtz billows in two spatial dimensions. *J. Atmos. Sci.*, **42**, 1321–1339.

Klaassen, G. P. and W. R. Peltier, 1985b: The onset of turbulence in finite-amplitude Kelvin-Helmholtz billows. *J. Fluid Mech.*, **155**, 1–35.

Klostermeyer, J., 1983: On parametric instabilities of finite-amplitude internal gravity waves. *J. Fluid Mech.*, **119**, 367–377.

Lehoucq, R. B., D. C. Sorensen, and C. Yang, 1998: *ARPACK Users' Guide: Solution of large-scale eigenvalue problems with implicitly restarted Arnoldi methods.* SIAM, 160 pp.

Lelong, M.-P. and T. J. Dunkerton, 1998a: Inertia-gravity wave breaking in three dimensions. Part I: Convectively stable waves. *J. Atmos. Sci.*, **55**, 2473–2488.

Lelong, M.-P. and T. J. Dunkerton, 1998b: Inertia-gravity wave breaking in three dimensions. Part II: Convectively unstable waves. *J. Atmos. Sci.*, **55**, 2489–2501.

Lindzen, R. S., 1981: Turbulence and stress owing to gravity wave and tidal breakdown. *J. Geophys. Res.*, **86**, 9707–9714.

Lindzen, R. S. and J. R. Holton, 1968: A theory of the quasi-biennial oscillation. *J. Atmos. Sci.*, **25**, 1095–1107.

McLandress, C., 1998: On the importance of gravity waves in the middle atmosphere and their parameterization in general circulation models. *J. Atmos. Sol.-Terr. Phy.*, **60**, 1357–1383.

Mied, R. P., 1976: The occurrence of parametric instabilities in finite amplitude internal gravity waves. *J. Fluid Mech.*, **78**, 763–784.

Miles, J. W., 1961: On the stability of heterogeneous shear flows. *J. Fluid Mech.*, **10**, 496–508.

Müller, P., 1976: On the diffusion of momentum and mass by internal gravity waves. *J. Fluid Mech.*, **77**, 789–823.

Nicolls, M. J., R. H. Varney, S. L. Vadas, P. A. Stamus, C. J. Heinselman, R. B. Cosgrove, and M. C. Kelley, 2010: Influence of an inertia-gravity wave on mesospheric dynamics: A case study with the Poker Flat Incoherent Scatter Radar. *J. Geophys. Res.*, **115**, D00N02, doi:10.1029/2010JD014042.

Yau, K. H., G. P. Klaassen, and L. J. Sonmor, 2004: Principal instabilities of large amplitude inertio-gravity waves. *Phys. Fluids*, **16**, 936–951.

List of Tables

	Statically Unstable IGW	Statically Stable IGW
IGW amplitude with respect to static instability	$a = 1.2$ ($\hat{u} = 29$ m s^{-1})	$a = 0.86$ ($\hat{u} = 21$ m s^{-1})
IGW wavelength, period	6 km, 8 h	6 km, 8 h
Primary perturbation	trans. NM: $\lambda_y = 7.943$ km para. NM: $\lambda_\xi = 501$ m ampl. $E^{\max}_{\text{pert}}/E_{\text{IGW}} = 5\%$	trans. SV: $\lambda_y = 3.162$ km ampl. $E^{\max}_{\text{pert}}/E_{\text{IGW}} = 10\%$
Resolution of nonlinear 2.5D simulation ($nx_\parallel \times n\phi$)	trans. NM: 1152×1152 para. NM: 288×2304	trans. SV: 1152×2304
Resolution for secondary singular vector calculation ($nx_\parallel \times n\phi$)	128×512	128×512
Wavelengths of leading secondary perturbations	trans. NM: $\lambda_\xi = 150$ m, 800 m para. NM: $\lambda_y = 270$ m	$\lambda_\xi = 485$ m, ∞

TABLE 1. Summary of model parameters.

List of Figures

5 Left: Growth factor of leading secondary singular vectors versus wavelength in the ξ direction for the basic state consisting of the statically unstable inertia-gravity wave perturbed by its leading transverse normal mode. Filled diamonds represent the leading 20 singular vectors at $\lambda_\xi = 150$ m and $\lambda_\xi = 800$ m. Right: Growth factors for an ensemble of randomly initialized integrations with heavy dashed line representing the ensemble mean. 40

6 Contours of perturbation vertical velocity amplitude $\hat{w}'_\zeta$ for the leading secondary singular vector (with $\lambda_\xi = 150$ m) of the perturbed statically unstable IGW over the basic state buoyancy field (shading, cf. upper- and middle-left panels of Fig. 2) at the initial time, half way to the optimization time and at the optimization time. Initially concentrated near maximum negative buoyancy gradient, the perturbation migrates in space with time due to advection by the basic state V and W_ζ fields. Contours of $\hat{w}'_\zeta$ are in increments of 20% of the maximum value at the corresponding time (amplitudes are increasing roughly exponentially with time). Black (white) contours represent positive (negative) values. 41

7 Energy conversion rates versus time for $\lambda_\xi = 150$ m leading singular vector (left) and random initialized integrations (right). Curves represent total perturbation energy growth, growth or decay due to shear in V (rvmean), shear in U_ξ (rumean), and gradients of B (rbmean), and decay due to viscosity and diffusion (dissip). All curves are normalized by the total perturbation energy. In the right panel, error bars represent the standard deviation about the mean over the ensemble of integrations. 42

8 As in Fig. 7 but for the $\lambda_\xi = 800$ m leading singular vector (left), the second-leading singular vector (middle) and the randomly initialized integrations (right). 43

15 Statically stable IGW case. Energy conversion rate density involving gradients of B (left), shear in U_ξ (centre), and shear in V (right) at the optimization time for a randomly initialized integration (bottom) and the same initial condition projected onto the leading singular vectors (top). Shading is scaled so as to show the sign (light positive, dark negative) and spatial distribution of each energy conversion mechanism but not the relative magnitudes of the three contributions. 50

16 Fraction of final perturbation energy of randomly initialized integrations not contained in the projection onto the leading 20 singular vectors. Plotted is the mean of $\sqrt{(E'_{total} - E'_n)/E'_{total}}$, where E'_n is the energy contained in the projection onto the leading n singular vectors, over an ensemble of 50 randomly initialized integrations. Error bars indicate standard deviation about the mean. 51

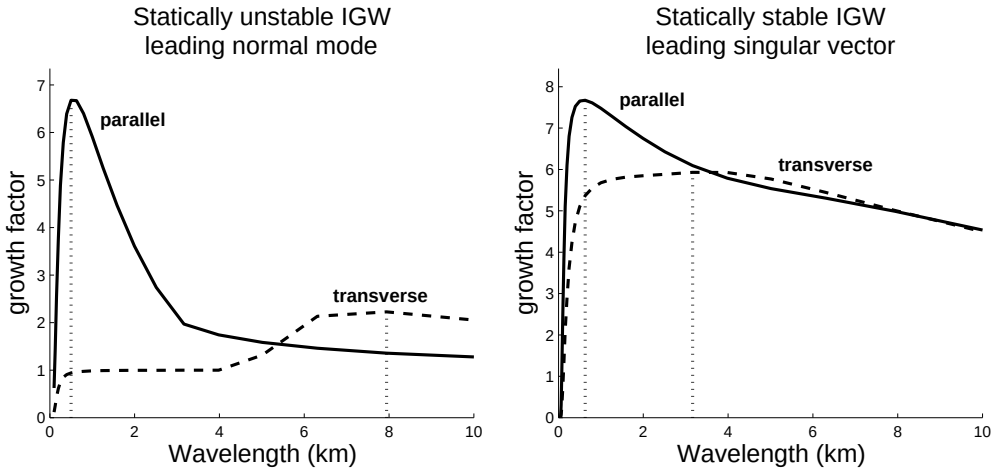

FIG. 1. Growth factor after 5 minutes of leading normal mode perturbations to statically unstable IGW (left) and singular vector perturbations to statically stable IGW (right). Growth factors of parallel perturbations (solid lines, varying in the ξ direction) and transverse pertubations (dashed lines, varying in the y direction) are shown.

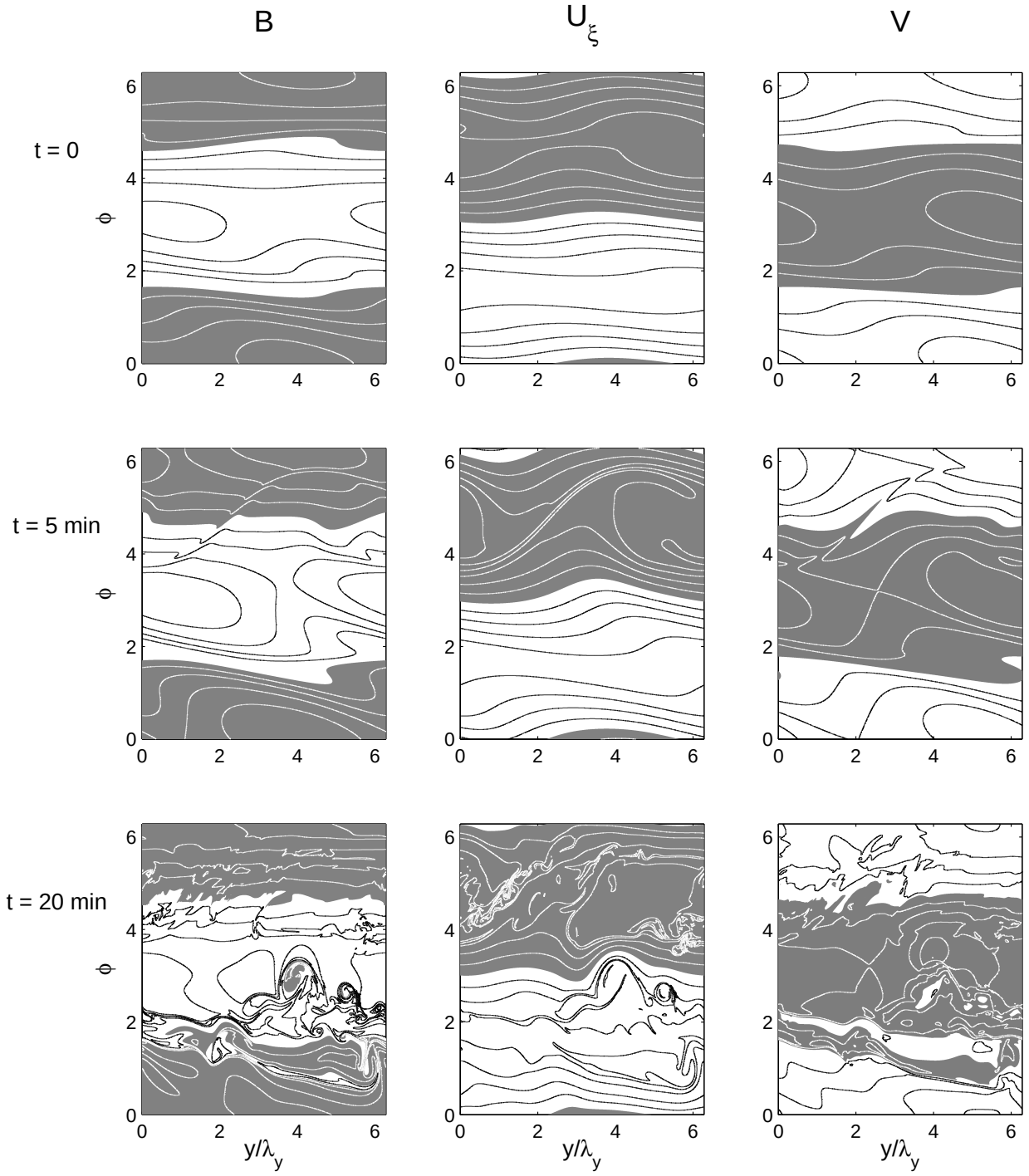

FIG. 2. Buoyancy B, parallel velocity U_ξ and transverse velocity V at the initial time, after five minutes, and after 20 minutes of a nonlinear integration of the statically unstable IGW perturbed by its leading transverse normal mode. Vertical axis is ϕ and horizontal axis is y/λ_y, where $\lambda_y = 7.943$ km is the wavelength of the primary perturbation. Positive values represented by black contours on white background and negative values by white contours on shaded background. Contour intervals are 0.12 m s^{-2} for B, 6.7 m s^{-1} for U_ξ and 6.0 m s^{-1} for V.

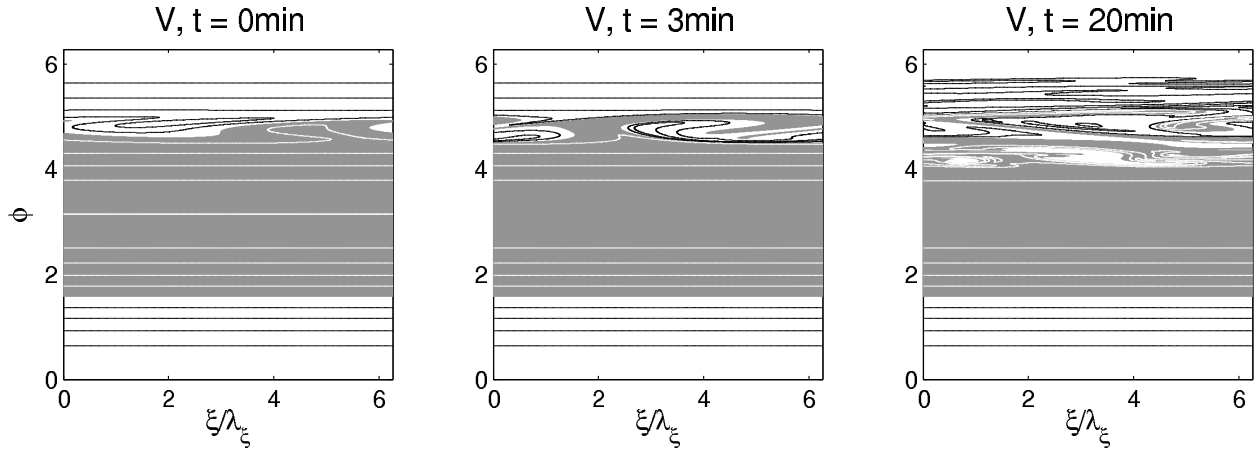

FIG. 3. Transverse velocity V as a function of ξ and ϕ at the initial time, after three minutes, and after 20 minutes of a nonlinear integration of the statically unstable IGW perturbed by its leading parallel normal mode, which has wavelength $\lambda_\xi = 501$ m. Positive values represented by black contours on white background and negative values by white contours on shaded background. Contour intervals are 3.6 m s^{-1}.

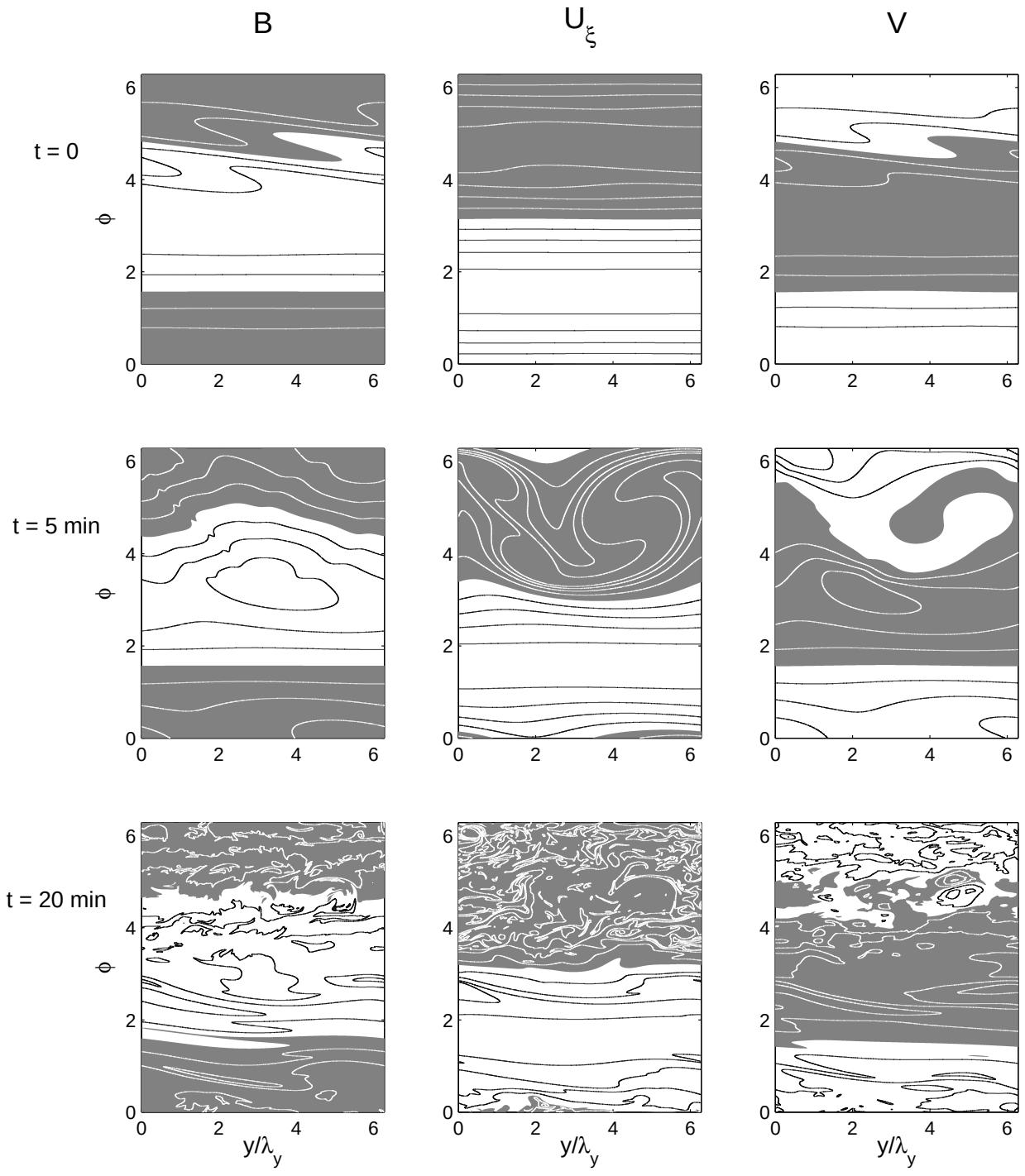

FIG. 4. As in Fig. 2 but for the statically stable IGW perturbed by its leading transverse singular vector. Contour intervals are 0.06 m s^{-2} for B and 2.3 m s^{-1} for U_ξ and V.

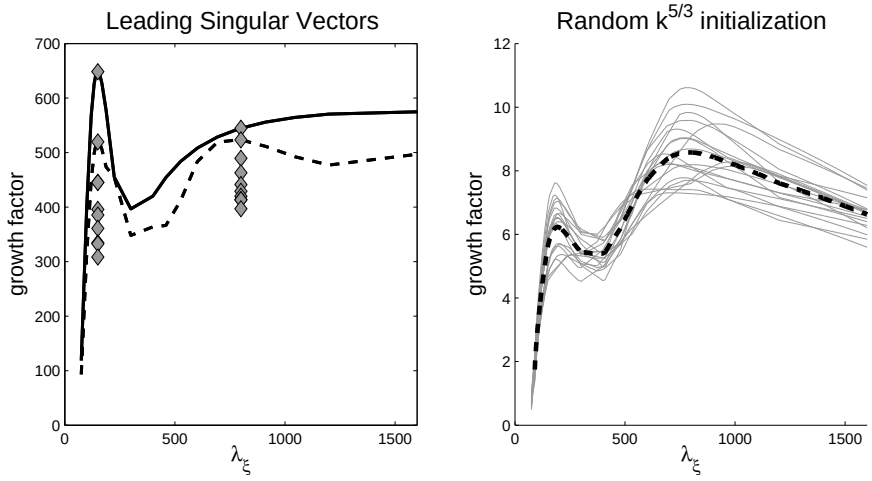

FIG. 5. Left: Growth factor of leading secondary singular vectors versus wavelength in the ξ direction for the basic state consisting of the statically unstable inertia-gravity wave perturbed by its leading transverse normal mode. Filled diamonds represent the leading 20 singular vectors at $\lambda_\xi = 150$ m and $\lambda_\xi = 800$ m. Right: Growth factors for an ensemble of randomly initialized integrations with heavy dashed line representing the ensemble mean.

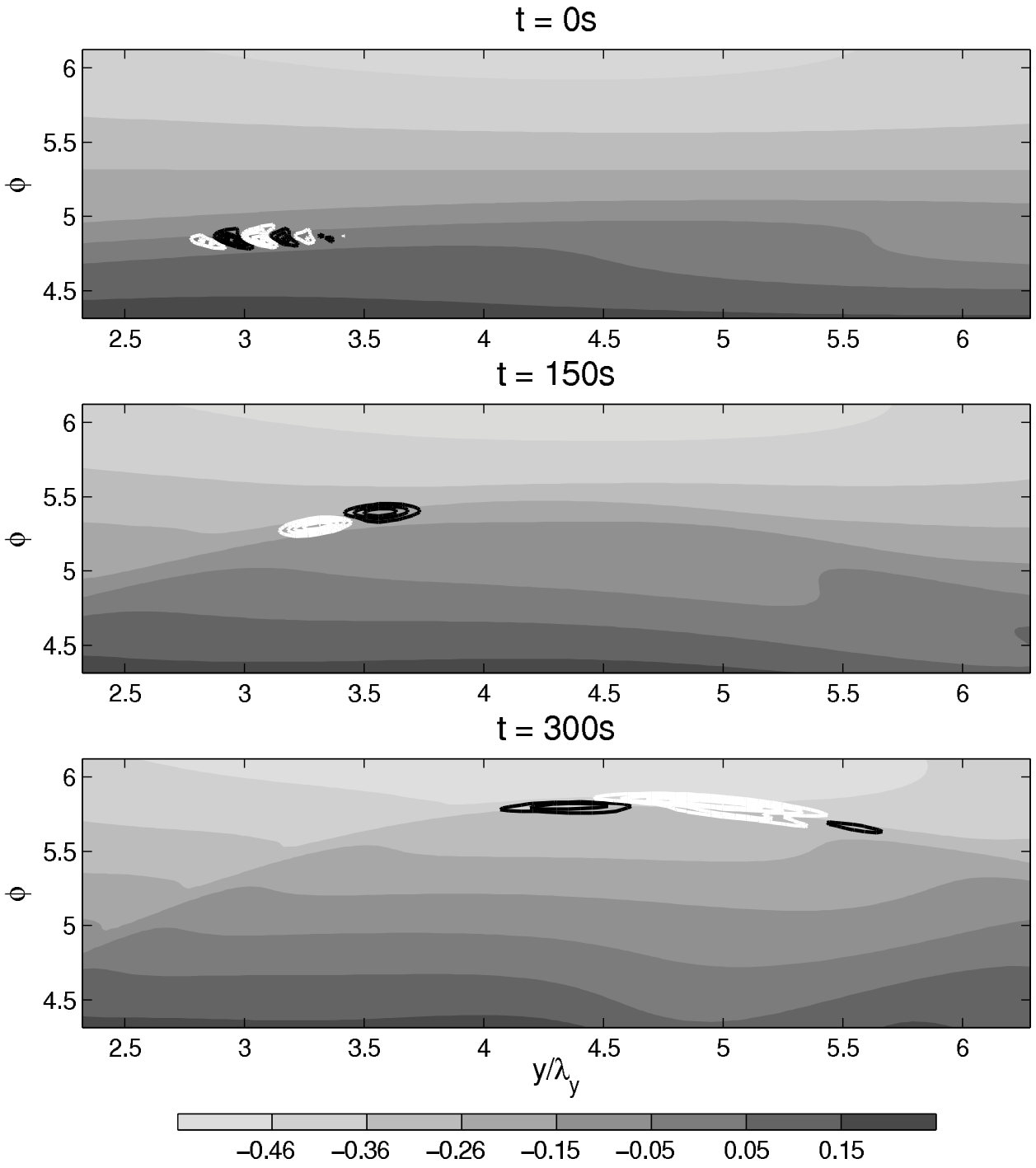

FIG. 6. Contours of perturbation vertical velocity amplitude $\hat{w}'_\zeta$ for the leading secondary singular vector (with $\lambda_\xi = 150$ m) of the perturbed statically unstable IGW over the basic state buoyancy field (shading, cf. upper- and middle-left panels of Fig. 2) at the initial time, half way to the optimization time and at the optimization time. Initially concentrated near maximum negative buoyancy gradient, the perturbation migrates in space with time due to advection by the basic state V and W_ζ fields. Contours of $\hat{w}'_\zeta$ are in increments of 20% of the maximum value at the corresponding time (amplitudes are increasing roughly exponentially with time). Black (white) contours represent positive (negative) values.

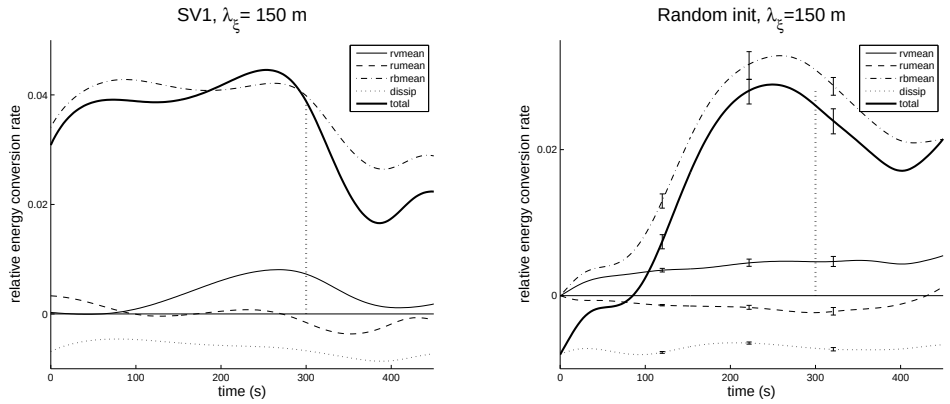

FIG. 7. Energy conversion rates versus time for $\lambda_\xi = 150$ m leading singular vector (left) and random initialized integrations (right). Curves represent total perturbation energy growth, growth or decay due to shear in V (rvmean), shear in U_ξ (rumean), and gradients of B (rbmean), and decay due to viscosity and diffusion (dissip). All curves are normalized by the total perturbation energy. In the right panel, error bars represent the standard deviation about the mean over the ensemble of integrations.

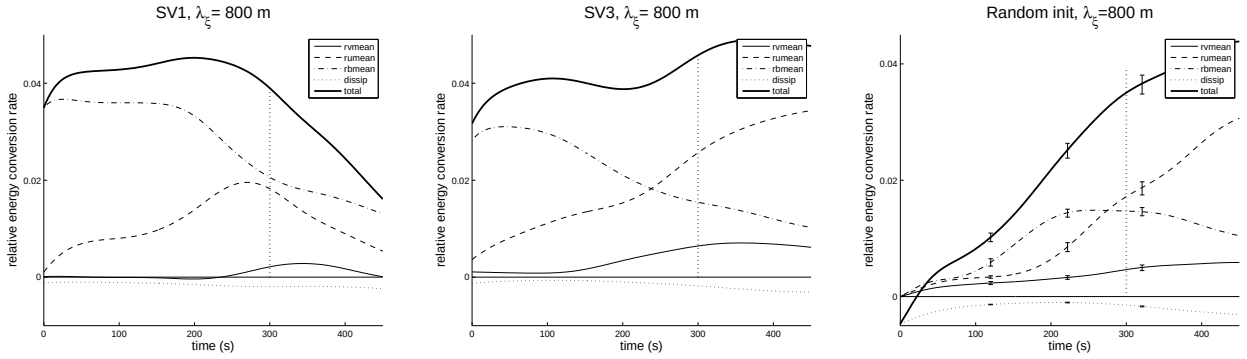

FIG. 8. As in Fig. 7 but for the $\lambda_\xi = 800$ m leading singular vector (left), the second-leading singular vector (middle) and the randomly initialized integrations (right).

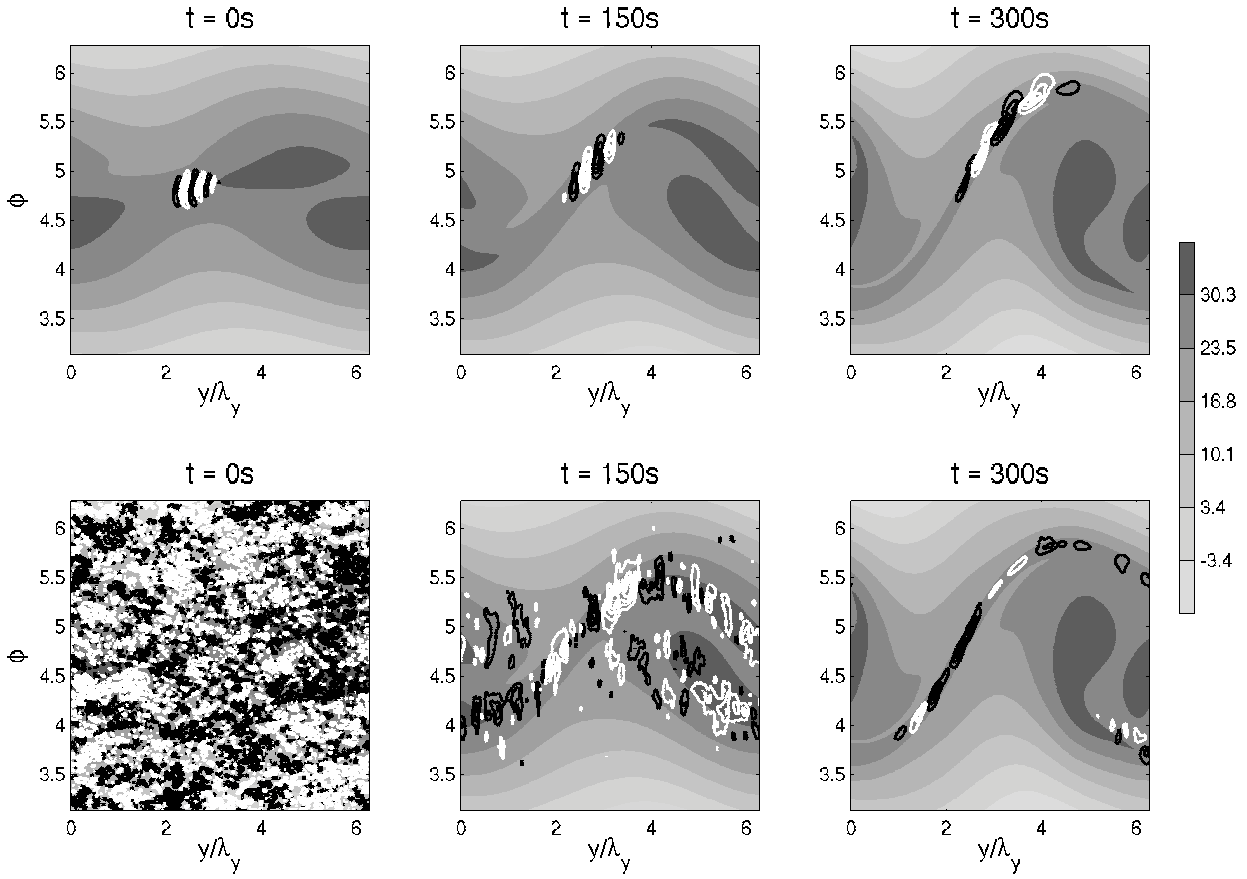

FIG. 9. Contours of perturbation vertical velocity amplitude $\hat{w}'_\zeta$ for secondary perturbations with $\lambda_\xi = 800$ m to the statically unstable IGW over the basic state parallel velocity field U_ξ (shading, cf. upper and middle centre panels in Fig. 2) at the initial time, half way to the optimization time and at the optimization time. Top row: second leading singular vector. Bottom row: randomly initialized integrations. Contours of $\hat{w}'_\zeta$ are as in Fig. 6.

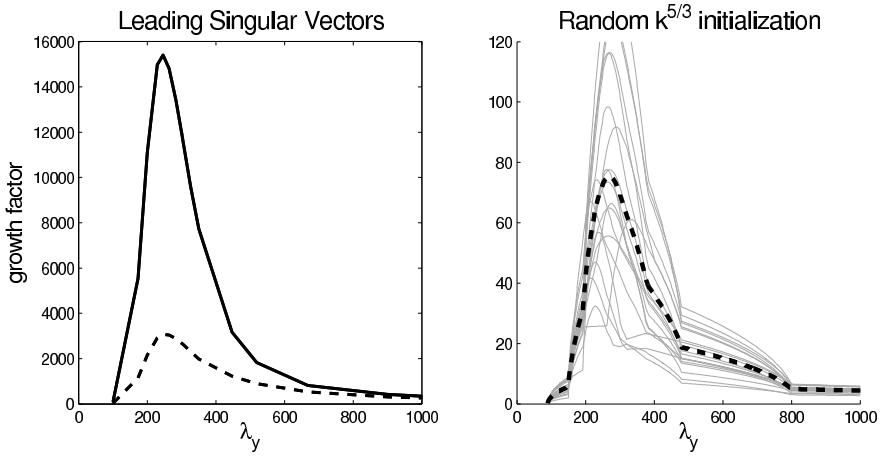

FIG. 10. Growth factor of leading secondary singular vectors (left) and randomly initialized integrations (right) versus wavelength in the y direction for the IGW perturbed by its leading parallel normal mode.

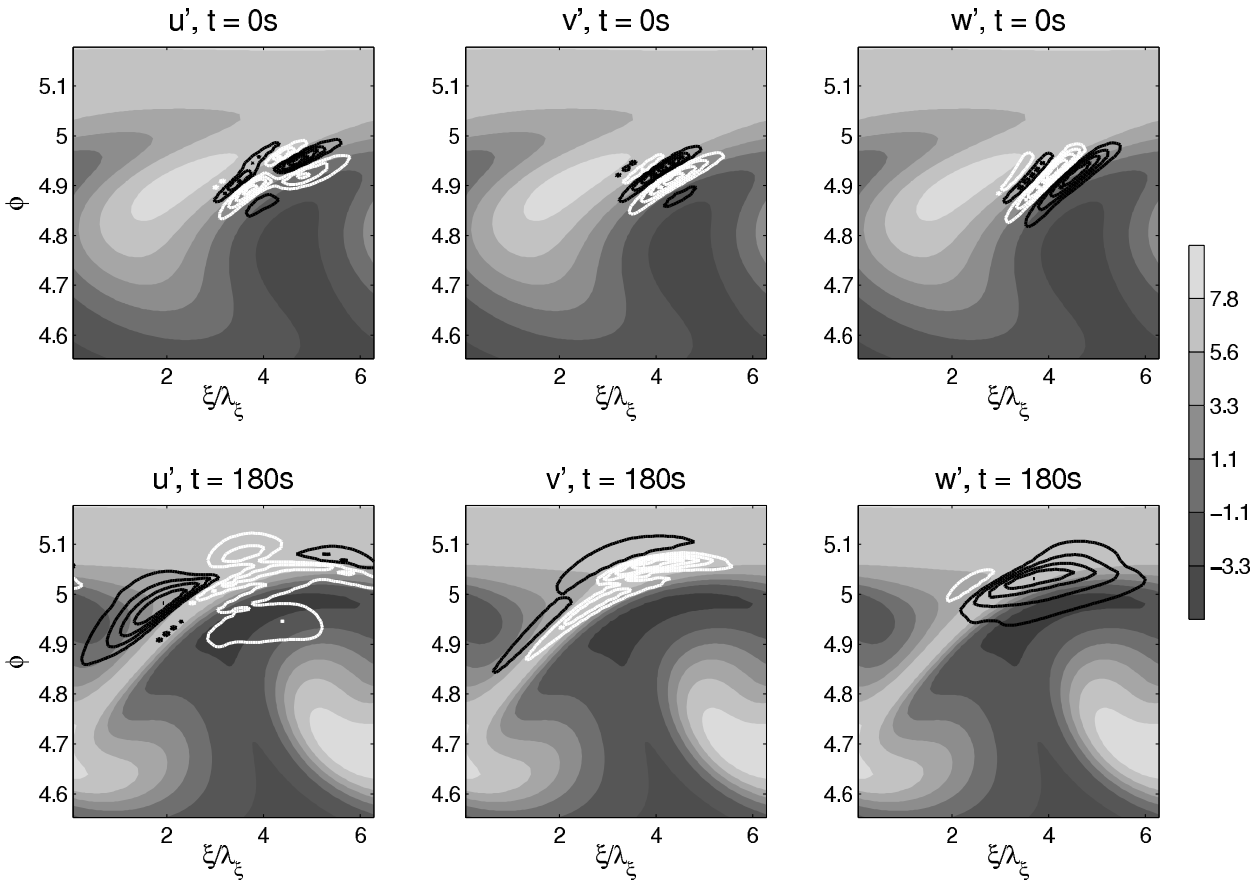

FIG. 11. Contours of perturbation velocity amplitude $\hat{u}'_\xi$, $\hat{v}'$, and $\hat{w}'_\zeta$, over basic state transverse velocity field V (shading) for secondary perturbations with $\lambda_y = 270$ m to the statically unstable IGW perturbed by its leading parallel normal mode at initial time (top row) and optimization time (bottom row). Contours are normalized by perturbation total energy as in Fig. 6.

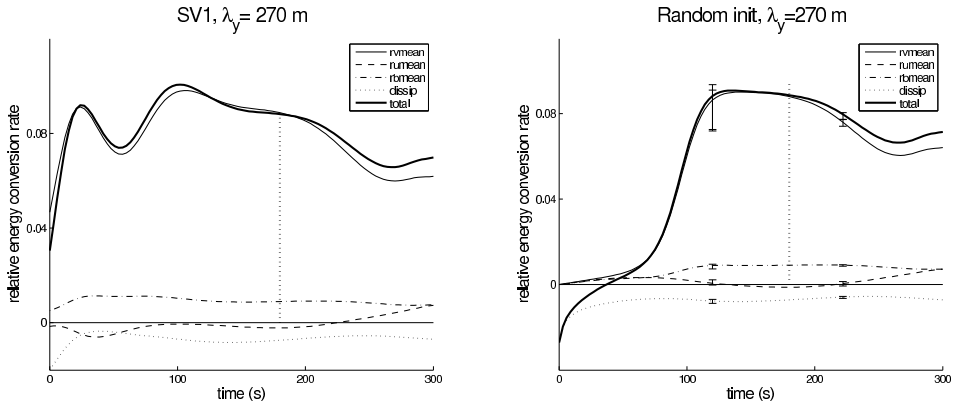

FIG. 12. As in Fig. 7 but for the IGW perturbed by its leading parallel normal mode: leading singular vector (left) and randomly initialized integrations (right) with $\lambda_y = 270$ m.

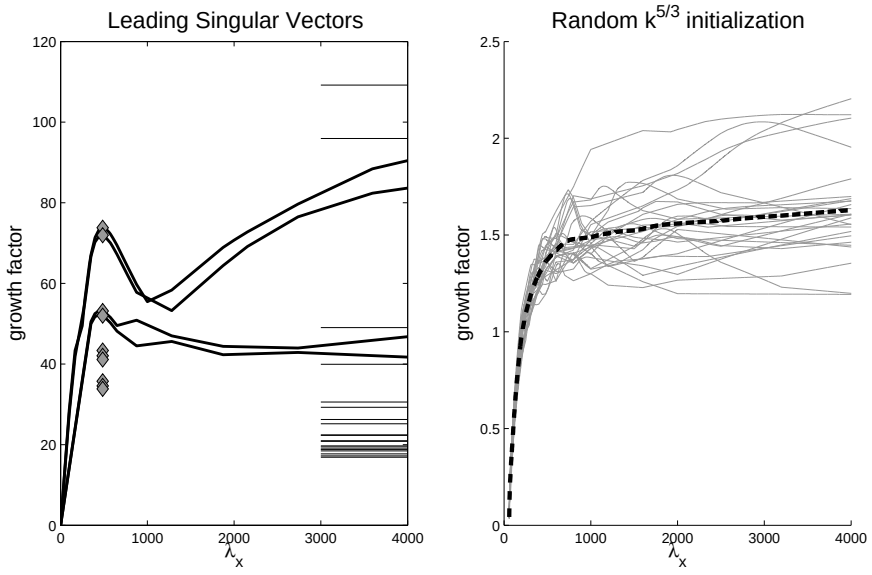

FIG. 13. As in Fig. 5 but for the perturbed statically stable IGW. Horizontal lines at right edge of left panel represent growth factors for $\lambda_\xi = \infty$.

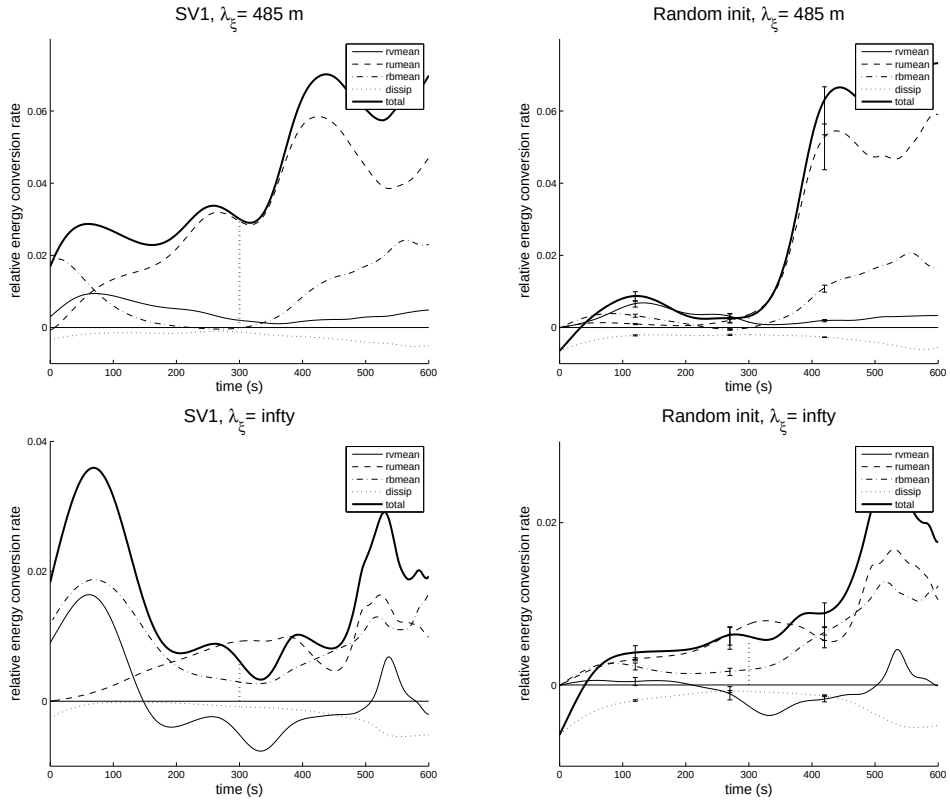

FIG. 14. As in Fig. 7 but for $\lambda_\xi = 485$ m (top row) and $\lambda_\xi = \infty$ (bottom row) and statically stable IGW.

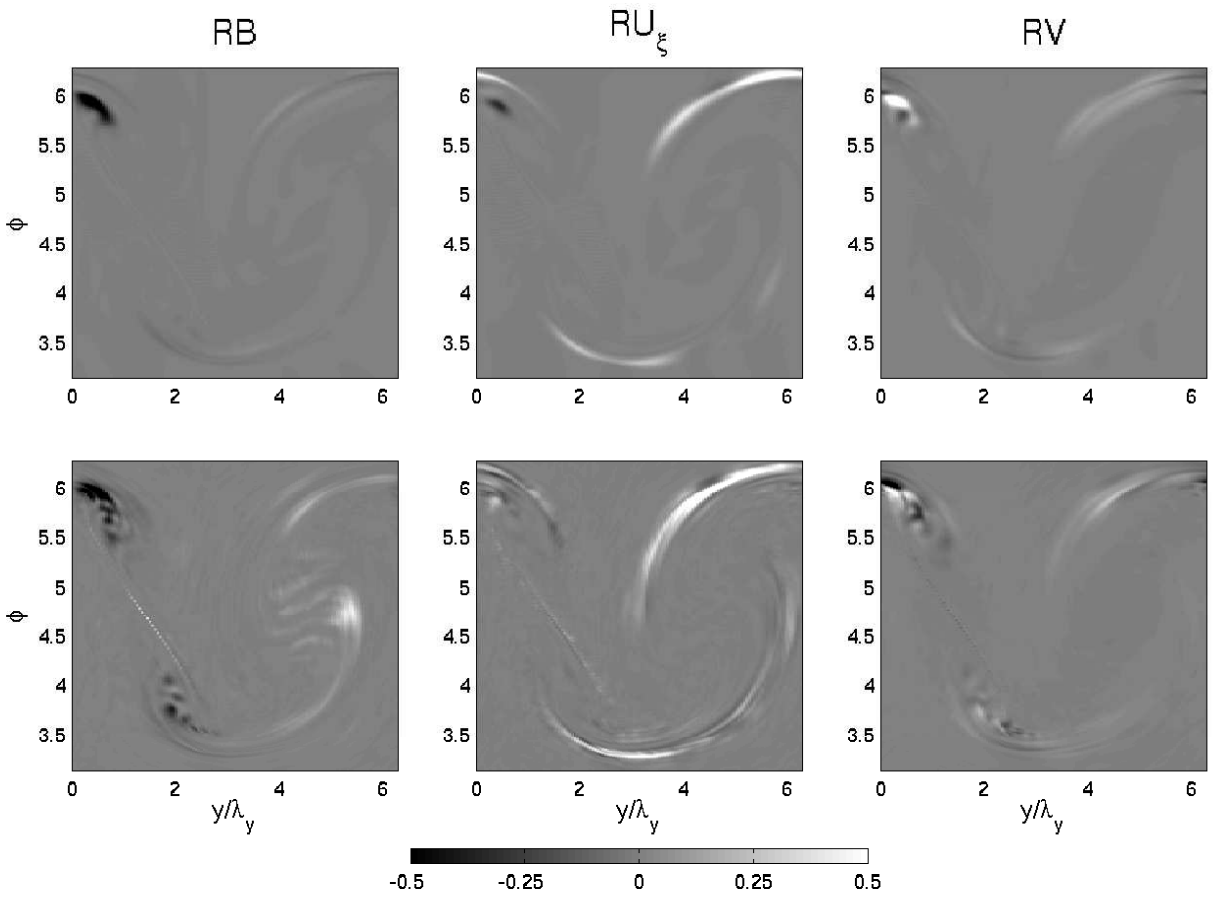

FIG. 15. Statically stable IGW case. Energy conversion rate density involving gradients of B (left), shear in U_ξ (centre), and shear in V (right) at the optimization time for a randomly initialized integration (bottom) and the same initial condition projected onto the leading singular vectors (top). Shading is scaled so as to show the sign (light positive, dark negative) and spatial distribution of each energy conversion mechanism but not the relative magnitudes of the three contributions.

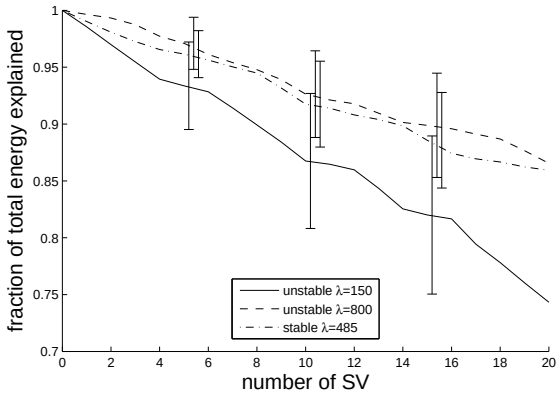

FIG. 16. Fraction of final perturbation energy of randomly initialized integrations not contained in the projection onto the leading 20 singular vectors. Plotted is the mean of $\sqrt{(E'_{total} - E'_n)/E'_{total}}$, where E'_n is the energy contained in the projection onto the leading n singular vectors, over an ensemble of 50 randomly initialized integrations. Error bars indicate standard deviation about the mean.